Title: Photocatalytic properties of BiOCl-TiO2 composites for phenol photodegradation

Authors: Dalia Sánchez-Rodríguez, María Guadalupe Méndez Medrano, Hynd Remita, Vladimir Escobar-Barrios

PII: S2213-3437(18)30062-9
DOI: https://doi.org/10.1016/j.jece.2018.01.061
Reference: JECE 2181

To appear in:

Received date: 4-9-2017
Revised date: 4-1-2018
Accepted date: 25-1-2018

Please cite this article as: Dalia Sánchez-Rodríguez, María Guadalupe Méndez Medrano, Hynd Remita, Vladimir Escobar-Barrios, Photocatalytic properties of BiOCl-TiO2 composites for phenol photodegradation, Journal of Environmental Chemical Engineering https://doi.org/10.1016/j.jece.2018.01.061

Photocatalytic properties of BiOCl-TiO_2 composites for Phenol Photodegradation

Dalia Sánchez-Rodríguez [1], María Guadalupe Méndez Medrano [2], Hynd Remita [2], Vladimir Escobar-Barrios [1]*

[1] Departamento de Materiales Avanzados, Instituto Potosino de Investigación Científica y Tecnológica (IPICYT), San Luis Potosí, SLP, CP. 78216, México.
[2] Laboratoire de Chimie Physique, Université Paris-Sud, Université Paris-Saclay, CNRS-UMR 8000, 91400, Orsay, France
* Corresponding author: vladimir.escobar@ipicyt.edu.mx

Graphical Abstracts

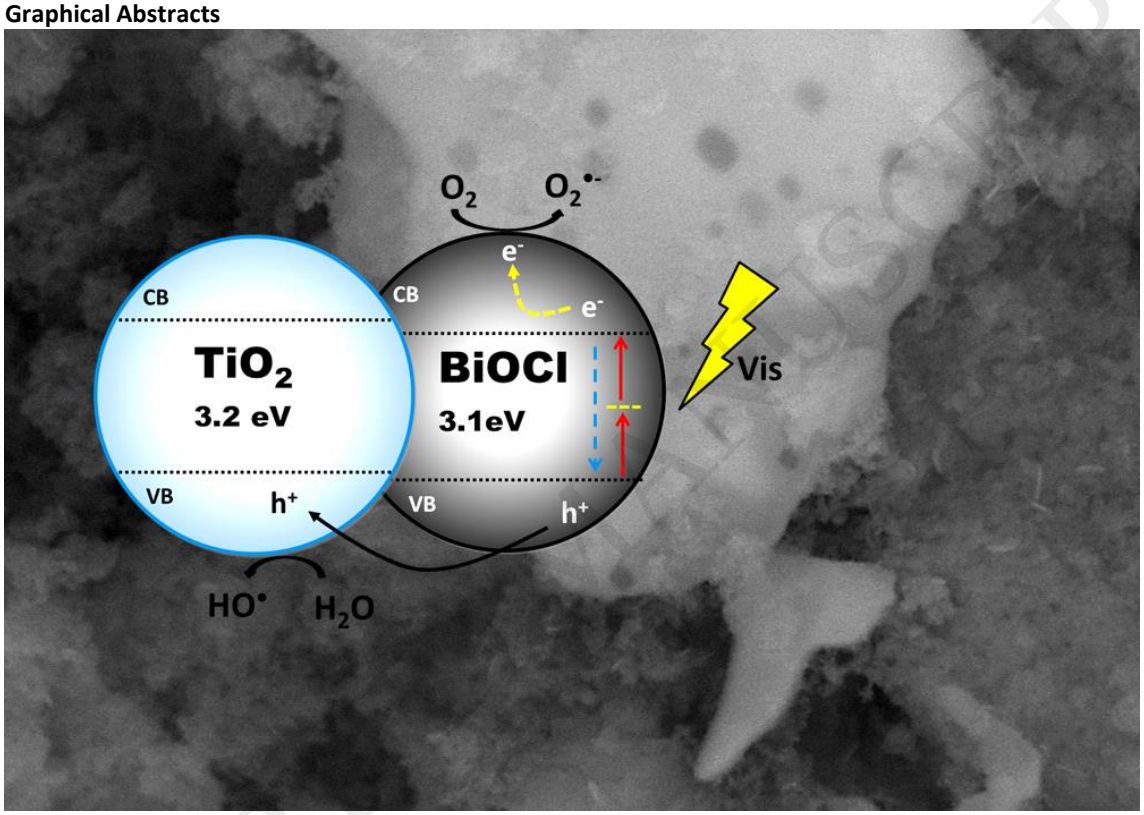

Highlights

- Composite BiOCl-TiO_2 is effective for photodegradation of phenol under visible light.
- The particle size of BiOCl has an important effect on its photocatalytic performance.
- It is proposed that a donor level below the conduction band is generated.
- The BiOCl-TiO2 is better than pure TiO2 or BiOCl for phenol photodegradation.

Abstract

BiOCl-TiO_2 composites were synthesized by sol-gel method; using two commercial BiOCl (P2600 and SB) with different BiOCl-TiO_2 weight ratios. They were characterized by different techniques such as X-ray diffraction (XRD), electron microscopy (SEM, HRTEM and TEM), Fourier transform infrared (FTIR), X-ray photoelectron spectroscopy (XPS), time resolved micro-wave conductivity (TRMC) and UV-vis diffuse reflectance spectroscopy (UV-DRS). In addition, these composites (BiOCl-TiO_2) were evaluated for the photodegradation of phenol (50 mgL^{-1}) under visible irradiation (λ>450 nm). The results showed effective phenol degradation with the PTi-75 composite, which has 75% by weight of TiO_2, obtaining up to 40% of degradation during 6 h of reaction. The SEM analysis showed that micro-sheets of BiOCl are irregularly embedded on agglomerates of TiO_2 nanoparticles. A mechanism was proposed, which considers the excitation by the overlap of the BiOCl-TiO_2 bands; where the TiO_2 has a conduction band more electronegative than that of BiOCl, allowing that TiO_2 electron of the conduction band can be transferred to conduction band of BiOCl; while the holes present in the valence band of BiOCl can be moved to TiO_2 valence band preventing the electron-holes recombination.

Keywords: BiOCl, TiO_2, Photocatalysis, Phenol, Visible light

1. Introduction

In recent decades the photocatalytic process has been widely used in areas such as the treatment of wastewater and air [1–3], self-surface cleaning [4], reduction of CO_2 [5–7] and for the production of H_2 [8,9]. Recently, part of the photocatalysis research has focused on the development of photocatalysts that have activity under visible irradiation and low recombination of the photogenerated electron-hole pairs. Thus, investigations have explored and studied different compounds, such as bismuth oxyhalides (BIOX; X = Cl, Br and I), and particularly the bismuth oxychloride (BiOCI) [10–20]. The BiOCl has a tetragonal structure constituted by sheets of [Cl-Bi-O-Bi-Cl], and an electric field is generated by inner layers $[Bi2O_2]^+$ which interacts with chlorine ions (Cl^-) by Van der Waals forces. This induces higher separation of photogenerated electron-hole pairs, and consequently, an improvement of the photocatalytic activity [10,13,21]. The band gap of BiOCl is in the range of 3.2 – 3.4 eV, therefore its photocatalytic activity is high under UV light.

The BiOCl (a p-type semiconductor) exhibits a remarkable photocatalytic performance for degradation of dyes under UV irradiation [10,11,13,22–24]. Similar work was performed for dye degradation using visible irradiation, determining that degradation proceeded by photosensitization process [10].

Thus, one of the strategies proposed in some studies is the development of composite materials based on BiOCl combined with different materials to improve its photocatalytic activity under visible light. Among the used materials for BiOCl modification are metals BiOCl-Ag [25–27], BiOCl-Fe[28], carbonaceous-based materials Graphene-BiOCl [29–31], and also hetero-junctions with other photocatalysts such as Bi_2S_3-BiOCl [32], BiOCl-Bi_2O_3 [33], BiOCl-$Bi_2O_2CO_3$ [34] and BiOCl-TiO_2 [35–41].

The hetero-junction between a low Fermi energy p-type semiconductor (BiOCl) and a high-energy n-type semiconductor (TiO_2) facilitates to reduce, or even to eliminate, the electron-hole recombination due to the binding of the internal electric field between both semiconductors.

There are reports about BiOCl-TiO_2 nanocomposites with good photocatalytic activity under UV irradiation [35,37,39,41] and sunlight [40], however the mechanism is not well understood. In this study, the synthesis of BiOCl-TiO_2 composite materials by the sol-gel method using two industrial BiOCl samples is presented and discussed. The obtained composites were evaluated under visible irradiation for degradation of phenol, used as a model pollutant. The characterization of the materials, in terms of their morphology, crystal structure and its correlation with the photocatalytic activity are discussed in detail. The charge carrier dynamic involved in the hetero-junction was studied by time resolved microwave conductivity. Finally, a mechanism for the photodegradation process is proposed.

2. Experimental

2.1. Materials

Two Commercial BiOCl samples were obtained from Farmaquimia S.A. (México). The samples were named as Pearl 2600 (P2600) and Satin B (SB). The Pearl 2600 sample has particle size of 2-10 μm, with rough texture and subtle sheen, in addition its contact angle is 134°, and then it is considered as hydrophobic. Satin B is a fine powder with

particle size of 1-20 μm and some opacity, with low hydrophobicity (contact angle of 23°). All other products used, titanium isopropoxide ($Ti(OCH(CH_3)_2)_4$, purity ≈ 97%), anhydrous ethanol (CH_3CH_2OH, purity ≈ 97%) and phenol (C_6H_5OH, purity ≈ 99%) were purchased from Sigma-Aldrich. Deionized water was obtained by a Tri-pure system (conductivity 18.4 MΩ). The reagents were used as received, that is, they were not treated in any way prior to be used.

2.2. Preparation of BiOCl-TiO_2 composites

The synthesis of BiOCl-TiO_2 composite materials was carried out by the sol-gel method with different BiOCl-TiO_2 weight ratios as is reported in the Table 1. The different composites were named as PTi-X or STi-X, where X is the percentage of TiO_2 in each sample, Ti is from TiO_2 and P or S is for the BiOCl sample, P for Pearl 2600 and S for Satin B. First, a suspension of ethanol (5.5 mL), deionized water (5.5mL) and BiOCl samples was prepared, under constant agitation. Subsequently, 1 mL of the solution of titanium isopropoxide $Ti(OCH(CH_3)_2)_4$ and 4.5 mL of anhydrous ethanol was added drop wise to form a gel. The gel was placed in the oven in a closed bottle at 80 °C for 24 h. Subsequently, the samples were washed with ethanol and dried at 110 °C, and finally their calcination was held at 450 °C for 4h with a heating ramp of 5°C min^{-1}.

2.3. Characterization

The crystal structure of the synthesized photocatalysts was analyzed by X-ray diffraction (XRD) using a DX8 advance diffractometer (Brüker) with: Cu Kα radiation, 35 kV, 25 mA, λ = 0.15418 nm over the 2θ range of 10° to 80° in a step of 0.02°s^{-1}.

The analysis of surface morphology and microstructure of the samples was carried out by a QUANTA 200 environmental scanning electron microscope equipped with an energy-dispersive X-ray spectroscope (EDS).

The high-resolution transmission electron microscopy (HRTEM) and transmission electron microscopy (TEM) imagines were carried out using a Tecnai F30 microscope (FEI) with tungsten field emission gun at 300 keV.

The functional groups were determined by Fourier transform infrared spectroscopy using a Thermo Nicolet 6700 spectrophotometer in a range from 500 to 3600 cm^{-1} with 124 scans. In this case, the samples were prepared in tablet form with potassium bromide (KBr).

The bandwidth (band gap) was obtained using a spectrophotometer model 5E (Cary) with a diffuse reflection area of 4/5. The baseline was obtained using poly(tetrafluoroethylene).

The characterization of the oxidation states was conducted by photoelectron spectroscopy emitted by X-ray (XPS) PHI VersaProbre II): The calibration of the position of the peaks of the elements was done with C1s at 284.6 eV.

Charge carrier dynamics was studied by time resolved microwave conductivity (TRMC). The sample was placed inside a waveguide, and then it was irradiated by a laser of Nd:YAG with an optical parametric oscillator (OPO) EKSPLA, NT342B, tunable between 220 to 2000 nm. The study was performed at 455 nm. The principle of this technique is the measurement of the microwave power reflected by the semiconductor when it is irradiated with the pulsed laser. A diode detector converted the signal into voltage for input to the oscilloscope. The conductivity of the sample is obtained, due to the variance created by the incident and the reflected microwaves power provides the absorbed microwaves power by the sample (ΔP) which is directly proportional to the variation of the conductance ($\Delta\sigma$) induced by the laser as is shown in the following equation 1:

Eq. 1 $$\frac{\Delta P(t)}{P} = A\Delta\sigma(t) = A\mu i\Delta ni(t)$$

Where, $\Delta ni(t)$ is the number of excess charge-carriers *i* at time *t* and μi is the mobility of charge carrier. The sensitivity factor *A* is independent on time, but depends on the microwave frequency and on the conductivity of the sample.

2.4. Photocatalytic activity

The photocatalytic properties of BiOCl-TiO_2 composites were evaluated by degradation of phenol with 50 mgL^{-1} initial concentration and 1 gL^{-1} of BiOCl-TiO_2 composite. The experiments were performed using a quartz reactor (volume of 3.5 mL) where the solution was irradiated with a xenon lamp (Oriel 300 W) using a filter (AM-32603-1, Lot-Oriel λ> 450 nm) for visible light experiments. Aliquots were taken every few minutes, and they were centrifuged for 10 minutes. After being centrifuged, the clear solution was analyzed by high performance liquid chromatography (HPLC) using a C18 column with a mobile phase of acetonitrile-water (25-75 %), with a flow of 0.5 mL min^{-1}.

3. Results and discussion

3.1. Crystallinity of BiOCl-TiO_2 composites

Figure 1 shows a typical XRD pattern of the different BiOCl-TiO_2 composites, which could be indexed to tetragonal phase BiOCl (JCPDS no. 06-0249, space group: P4/nmm, a = b = 0.389 nm and c = 0.737 nm), while XRD pattern of TiO_2 sample corresponds to anatase TiO_2 (JCPDS no. 21-1272, space group I41/amd, a = b = 0.378 nm and c = 0.951 nm). There are no other peaks or shift of peaks observed in the patterns. The peaks of higher intensity are in the planes (001), (101), (110) and (102) corresponding to 2θ = 11.9, 25.9, 32.5 and 33.5, respectively. The diffraction peak intensities of (001) and (002) planes become higher, indicating that pure BiOCl (P2600 and SB) should be favored to grow along the c-axis [001] orientations.

When the amount of TiO_2 increased to 75%, the peak (001) of BiOCl decreased and the peak (001) of TiO_2 increased, then probably an interaction between the phases of both photocatalysts was taking place. In the case of composites with low TiO_2 percentage (25 and 50 %), the peaks corresponding to such entity were not visible and just appeared those corresponding to BiOCl. The crystal size to pure BiOCl and pure TiO_2 has been calculated by using the Scherrer formula [42], where the size obtained was 36.2 nm for both BiOCl (P2600 and SB) and 6.5 nm for pure TiO_2. This result could be indicative that the crystal size of BiOCl is higher enough to screen the TiO_2, even at 50% by weight of it.

3.2. Electron Microscopy Analysis

The morphology of the BiOCl-TiO_2 composites was observed by SEM, TEM and HRTEM. Figure 2a) shows the SEM image of agglomerates of pure TiO_2 with size of 100 microns formed from small particles of 2.5 nm approximately of pure TiO_2 synthetized by method sol-gel. While the BiOCl (P2600) showed irregular morphology of agglomerates formed from overlapping flakes of 10-60 microns approximately

(Figure 2b), SB have a similar morphology to P2600 but with flakes of 9-34 microns (see Figure S1).

In both BiOCl-TiO_2 composites the agglomerates of TiO_2 nanoparticles exhibit BiOCl flakes embedded (Figures 2c and 2d), as well as TiO_2 scattered nanoparticles covering flakes of BiOCl as it is observed for PTi-75 sample (Figure 2e and 2f). This complete interaction between TiO_2 and BiOCl could promote a better separation of photocharges generated during the reaction and therefore a better photocatalytic activity. The increment of TiO_2 quantity decreases the amount of BiOCl flakes embedded into it (Figure S1).

In the EDS analysis by made to a fragment of the sample of P2600-TiO_2 (Figure 3) it was corroborated that the fragment of larger dimensions belonged to TiO_2 due to the high amount of titanium obtained (red area), compared to the analysis made in the area of small fragments (green area). In this area the signal related to Bismuth increased due to the higher BiOCl content in such area.

The TEM and HRTEM analysis were carried out on the composites PTi-75 and STi-50 since they exhibited the higher photocatalytic activity. The Figure 4 shows the respective micrographs for both samples.

The TEM images show that composites samples consist of elongated particles, corresponding to BiOCl (P2600 and SB), which are embedded on irregular agglomerates of TiO_2 nanoparticles (Figure 4a and 4c) as it was also observed in SEM images. The HRTEM microphotographs (Figure 4b and 4d) show an interplanar space of 0.73nm corresponding to the plane (001) of BiOCl, and a space of 0.29 nm corresponding to the (001) plane of anatase TiO_2, such planes coincide with those obtained by XRD (shown further). These micrographs somehow demonstrate that BiOCl-TiO_2 heterojunctions were successfully generated.

3.3. Fourier Transformed Infrared (FT-IR)

The FT-IR spectra for the composites along with the pure samples of BiOCl and TiO_2 are shown in Figure 5.

In the case of pure TiO_2 the broad absorption band at 581 cm^{-1} corresponds to Ti-O bond, also, the absorption bands at 3500 and 1600 cm^{-1} are associated with the vibrations of free water molecules, which may be due to the absorption of humidity during analysis and to carboxyl acid from used reactives during its synthesis, respectively.

For the pure BiOCl, the vibration at 538 cm^{-1} corresponds to Bi-O bond, which is characteristic for this compound. In addition, the signals at 2920, 1630 and 1376 cm^{-1} correspond to carboxyl and alkanes groups, which could be associated to residues of surfactant that are commonly used during preparation of the BiOCl, which is clearly observed for Satin B. It is necessary to clarify that these samples of BiOCl were obtained industrially (then, we do not know its method of synthesis), however, some reported methods of BiOCl synthesis use acetic acid[21] or ethylene glycol [43] in order to obtain well-defined structures of BiOCl. Then residues from such molecules could be also attributed to the mentioned signals. Thus, the samples could have interactions with water, by hydrogen bonds, and is why the broad band at 3400-3500 cm^{-1} appears for both BiOCl.

3.4. Diffuse Reflectance Spectroscopy UV-Vis

Figure 6 shows the diffuse reflectance spectra of samples of pure BiOCl, TiO_2 and BiOCl-TiO_2 composites. Pure BiOCl and pure TiO_2 samples showed absorption only in the UV region, while for P2600-TiO_2 composites not only present strong absorption in the UV region, but also the absorption was displaced to visible region, especially as the amount of TiO_2 increased, being the PTi-75 composite with the higher absorption for such series. In the case of SB-TIO_2 composites, the STi-50 composite showed the higher absorbance; this may be due to a good interaction between BiOCl and TiO_2 generating more stable hollow-electron pairs. The BiOCl present a potential energy in the valence band more positive than TiO_2; therefore, the band gap of TiO_2 is more electronegative, this interjuction between both photocatalysts to reduce the distance of electron during the excitation as is described in the mechanism photocatalytic proposed.

The optical absorption near the band edge follows the equation 2:

Eq. 2 $$\alpha h\nu = A(h\nu - Eg)^{\frac{n}{2}}$$

Where α, v, A, and Eg are the absorption coefficient, light frequency, a constant and energy bandwidth, respectively. The value of *n* depends on the type of optical transition of the semiconductor, $n = 1$ for a direct transition, while $n = 4$ for indirect transition. For BiOX the *n* value has been reported equal to 4 [44,45]. The bandwidth energy (Eg) of the samples was obtained by plotting BiOCl $(\alpha h\nu)^{1/2}$ versus Eg (shown on supplementary information Figure S2) when the X-axe is crossed. The Table 2 summarizes the deduced values of the bandgap of the different evaluated samples; corroborating a low energy bandwidth for PTi-75 and STi-50 composites. Thus, it would be expected that samples with a bandgap around 2.8 eV would have better catalytic performance in the visible region.

3.5. Photocatalytic Evaluation

Previous photocatalytic experiments, not shown here, were carried out using Rhodamine B (RhB, $1x10^{-4}$ M) in the presence of BiOCl (P2600 and SB) under visible light. The results obtained (Figures S3 and S4 of Supplementary Information) show an effective photodegradation process. Regarding the degradation kinetic, it is similar with UV light and Visible light for Pearl 2600.

Thus, it is concluded that these materials are non-active under visible light, and that degradation of RhB is mainly due to its sensitization in the presence of the semiconductor (ejection of electron from the excited RhB to the conduction band of the semiconductor leading to its further degradation, see Figure S4). From these previous experiments, it is expected that pure BiOCl exhibit very low photocatalytic activity under visible light. The TiO_2 is known to be active only under UV light because of its band gap, but the heterojunction of TiO_2 with other semiconductors as BiOCl could be an effective method to improve the excitation, and its photocatalytic activity, with visible irradiation.

The photocatalytic activity of the different TiO_2-BiOCl composites was evaluated during the degradation of phenol under visible irradiation (Figure 7). In the case of P2600-TiO_2 composites, the degradation percentage was increased as the amount of TiO_2 was increased. The highest photocatalytic activity was obtained with PTi-75,

which exhibited 43% of phenol degradation after 6 h of photocatalytic reaction (Figure 7-a). These results may be related to better absorbance obtained in the visible range due to the synergy between BiOCl and TiO_2, probably due to the overlap of their bands since they are intimately interacting.

The photocatalytic activity of SB-TiO_2 composites did not follow any trend, achieving 36% degradation of phenol with STi-50 composite, after 6 h (Figure 7-b). This difference in the phenol photodegradation percentage could be associated to the variation in size of the BiOCl, since SB is slightly smaller than P2600 and thus, considering that composites have almost the same quantity of each one, but different volume, then it is probable that SB generates more active sites that could promote recombination that decreased the photocatalytic activity. The photocatalytic activity is related with the band gap obtained previously in both composites (PTi-75 and STi-50, shown further), which allows greater photocatalytic activity under visible light.

Such results confirm that there is a synergistic interaction between BiOCl and TiO_2, which depends on morphology and proportion of BiOCl in each composite. The adequate percentage of TiO_2 in the composites depend of the characteristic of BiOCl, in this case the morphology, size and the hydrophobicity or hydrophilicity played an important role. For example for the P2600-TiO_2 composite the better photocatalytic activity was obtained with 75% of TiO_2 (PTi-75), maybe due to the hydrophobicity of BiOCl (contact angle of 134°) and the big size of agglomerates of BiOCl allowed a minor interaction with TiO_2 and therefore, it was necessary higher content of TiO_2. In the case of Satin-TiO_2 composites; they have smaller size and low hydrophobicity (contact angle of 23°), which led to obtain better photocatalytic activity with lower percentage of TiO_2 (STi-50) than PTi-75.

It is known that degradation of phenol under visible light is difficult, Ali et al (2017) worked with nanotubes of TiO_2 doped with Bismuth for the degradation of phenol ($50mgL^{-1}$) under visible light; they obtained a phenol's degradation of 17.5% by photocatalytic process and a 40.7 % with photoelectrocatalytic process in 8 hour [46], the percentage of degradation by photocatalytic process compared with this works is lower, even considering that the configuration and type of the semiconductor components were different. In Table 3 are some works about the phenol degradation. Note that concentration of photocatalyst, the initial phenol concentration the radiation type (UV or visible light) were different. Therefore, the time and percentage of

degradation were different and no direct contrast with this work is possible, however it give a general idea of the kind of work related with phenol photodegradation.

Regarding the use of BiOCl-TiO_2 for degradation of dyes under UV and visible light some authors have reported their findings [35,37,38,53,54]. However, in the case of phenol degradation Fangfang et al (2016) reported a degradation of 93% using BiOCl-TiO_2 in just 30 min under artificial solar light irradiation, however the concentration of phenol that they used was 10 mgL^{-1}, five times lower than the concentration used in this work, also in the solar light irradiation there is about 5% of UV light, which can participate in the photocatalyst process [55]. In addition, Ao et al (2014) worked with the degradation of phenol (5 mgL^{-1}) and the degradation was carried out easily under UV light [56]. As it can be see, there are not many studies of phenol photodegradation using BiOCl-TiO_2 composites and higher initial concentration of phenol as we report in this study.

3.6. X-ray Photoelectron Spectroscopy (XPS)

XPS analysis was used in order to determine the chemical composition and the electronic configuration of BiOCl-TiO_2 composites (Figure S5). In pure BiOCl was observed oxygen and bismuth as main elements. The oxygen peak was located at 529.6 eV which correspond to Bi-O bonds in $[Bi_2O_2]^{2+}$ slabs of BiOCl (Figure 8-a), two strong peaks located at 158.6 and 164 eV were observed and assigned to Bi $4f_{7/2}$ and Bi $4f_{5/2}$ from Bismuth (Figure 8-b). The difference between both Bi^{3+} signals (5.4 eV) is characteristic of BiOCl[55,57]. Regarding to pure TiO_2 (Figure 8-f) the signals at 458.2 and 463.6 eV correspond to Ti $2p_{1/2}$ and Ti $2p_{3/2}$, respectively. The difference between the two signals (5.4 eV) indicates the Ti^{4+} oxidation state and the oxygen peak was located to 529.6 eV, which is attributed to the Ti-O bands in TiO_2[34,40,58].

The elements present in PTi-75composites were Bismuth (Bi 4f), Chlorine (Cl 2p), Titanium (Ti 2p), Oxygen (O 1s) and Carbon (C 1s) (Figure S3). Figure 8-c, 8-d and 8-e show the high-resolution XPS spectra of titanium, oxygen and bismuth, respectively, for PTi-75 composite. In figure 8-c four peaks are observed; two peaks at 458.2 and 463.6 eV, which could be assigned to Ti^{4+} of Ti-O bond. The other two peaks observed at 456.7 eV and 467.0 eV could be due to a state of lower and high oxidation state of titanium, probably originates from the formation of Ti-O-Bi bond or Ti-Cl bond [54,59].

Likewise were observed four signals to bismuth. Two strong peaks located at 158.8 and 164.2 eV, which are assigned to Bi $4f_{7/2}$ and Bi $4f_{5/2}$ from Bi-O bond of BiOCl[55,57]. The others signals observed at 157.0 and 162.2 eV, would indicate the presence of Bi center with a lower vacancy valence (Bi^0), which can be attributed to the presence of oxygen vacancies. [16,34,58,60]. The O 1s peak at 529.6 eV should be ascribed to the Ti-O and Bi-O bonds, while the peak at 527.3 eV could be related to O-H bonds of the surface adsorbed water.

After the photodegradation, observed the same elements and peaks (Figure S6), so it can be said that these composites are stable.

For XPS spectra of samples STi-50 (see in Figure S5), it was observed likewise the presence of bismuth (Bi 4f), chlorine (Cl 2p), titanium (Ti 2p), oxygen (O 1s) and carbon (C 1s). The Figure 9-a-b shows the XPS spectra oxygen and bismuth of pure BiOCl. The signal corresponding to oxygen was observed at 529.4 eV, while the signals corresponding to bismuth were observed at 158.6 and 164.0 eV. These signals correspond to Bi 4f5/2 and Bi 4f1/2 assigned to Bi^{3+}. In the XPS spectrum of Bi 4f of STi-50 composite two signals appear at 157.1 and 162.5 eV corresponding to a lower binding energy associated to Bi^0. The O 1s peak at 527.9 and 529.9 eV should be ascribed to the Ti-O bond and Bi-O bonds of TiO_2 and BiOCl. For the XPS spectrum of Ti 2p four signals were observed at 459.1, 461.6, 467 and 469.9 eV (Figure 9-c) indicating the presence of titanium as Ti^{4+}, other peak was observed with lower binding energy probably originates from the formation of Ti-O-Bi bond or Ti-Cl bond as was described with PTi-75 composite. After the photodegradation, it is observed the deconvolution of oxygen in three peaks; they perhaps correspond to O-H bonds. Referring to Bi 4f and Ti 2p the same peaks are observed (Figure S7).

In both composites, it was observed different oxidation states for the present elements, due to the interaction between BiOCl and TiO_2, and even possibly due to other interactions between Ti and Bi with O by vacancies that may affect the photocatalytic activity.

3.7. Time-Resolved Microwave Conductivity (TRMC)

Charge carrier dynamics, which is a key factor in photocatalysis process, was studied by TRMC in the n-p heterojunction. The TRMC signals of the excited composites at the wavelength of 455 nm are shown in Figure 10. The main data provided by TRMC signals are: (i) the maximum value of the signal (I_{max}), which reflects the number of the excess charge carriers created by the pulsed laser, weighted by the mobility of the charge carriers and by the influence of charge-carrier decay processes during the excitation, and (ii) the decay of the signal I(t), which is related to the decrease of the excess electrons controlled by the trapping and the recombination process [61].

High intensity charge signals are observed for both pure BiOCl samples. The BiOCl exhibits an indirect band gap, it means that there is contribution of photon and phonon (quantum mechanical manifestation of thermal vibrations in the crystal lattice). The electrons can still be excited at relatively low energies to the conduction band due to the two-photon absorption on the indirect band gap semiconductors [62], explaining the generation of charge carriers under visible light [63,64]. The intense TRMC signal of BiOCl under visible light is due to the holes in the conduction band, which have more mobility compared to the electrons in the p-semiconductor. The decay of the TRMC signal is related to the recombination process (a vertical transition) and to the indirect transition that requires the intervention of a phonon due to the different values of the crystal momentum.

The catalytic results show that the produced holes and electron are not active in bare BiOCl during the photocatalytic process, probably due to the high recombination rate of the charge carriers. The Pearl 2600 displays a faster signal decay compared to Satin B. The TiO_2 presented a low intensity signal, confirming its low excitation under visible light because of its gap band value (3.2 eV), which inhibits its excitation under such light. However, the BiOCl-TiO_2 composites showed a higher charge generation (higher I_{max}) compared to bare TiO_2, but lower signal compared to pure BiOCl except for the PTi-25 and STi-25. Generation of high density of charge carriers leads to higher generation of reactive species such as $^{\bullet}OH$ and $O_2^{\bullet-}$, and therefore to a better photocatalytic activity.

The TRMC signals for the BiOCl-TiO_2 decrease due to the presence of TiO_2, which act as a holes trap. Thus, when the holes are transferred to TiO_2, they are much less mobile in this semiconductor, and the TRMC signals decrease under visible excitation. This

hole trapping by TiO_2 induces an increment in charge carrier separation retarding the recombination process, as shown in the scheme in the Figure 10-II, and a higher photocatalytic activity under visible light of the composite material takes place. It has to be pointed out that the energy band gap value and energy level positions of BiOX (X= Cl, Br, I) can change with size, shape and number of layers as is reported by Zhao and col. [65], and Li. [66] In our case, hole trapping by TiO_2 is observed in PTi-75 and STi-50 composites.

3.8. Contribution of electrons and holes to photocatalytic process

In order to establish the role of electrons and holes during the photocatalytic process of phenol degradation, under visible irradiation, such reaction was carried out in the presence of isopropanol (IPA 0.1 M) as a trap of holes, and in the presence of copper sulfate ($CuSO_4$,$1x10^{-5}$ M) as a trap of electron, using the PTi-75 composite. The Figure 11 shows the results of phenol degradation percentage with P2600-TiO_2 in presence of isopropanol or $CuSO_4$.

As shown in Figure 11, the phenol degradation efficiency in presence of IPA was 35%, indicating that •OH species (formed by the reaction of the hole with water) are not the main reactive species. Although, such species do participate in the photocatalytic reaction since they reduce the photocatalytic efficiency of the composite.

In the presence of $CuSO_4$, phenol degradation was only 8% after 12 h irradiation, confirming that electrons are strongly involved in photocatalytic activity, and this may be due to the generation of superoxide anions (formed by the reaction of electrons with oxygen).

3.9. Photocatalytic stability

In order to study the photocatalytic stability of PTi-75 and STi-50 composites, three reaction cycles were carried out, and after each reaction the composites were collected and dried before the next photocatalytic reaction. In the Figure 12 showed the photocatalytic process of PTi-25 and STi-50, along with the percentage of total organic carbon eliminated. All the cycles were carried out maintaining a constant photocatalyst

concentration of 1 gL^{-1}. The PTi-75 showed a 55% degradation of phenol after 12 h irradiation in the first cycle. Then, during the second cycle, showed a lower photodegradation of 37% of phenol and during the third cycle it was increased again to 44% of degradation (Fig. 12-a). It must be said that during the second cycle the contact between the composite and the solution along the reaction was not the same as the others cycles due to the fact that a certain quantity of photocatalyst was crusted on the reactor walls, since oxygen bubbles contributed to carry out the photocatalyst from the bulk solution toward the wall; therefore, the photocatalytic efficiency was reduced (See Figure S8).

For the STi-50 composite, in the first two cycles the phenol degradation was high and similar (44 and 39 % after 12 h irradiation), while in the third degradation cycle is lower (29%) as it can be seen in Figure 12-b). Therefore, the obtained photocatalysts, especially the P2600 based one, could be used up to three times with a reasonable efficiency during the Phenol photodegradation.

The percent of total organic carbon (TOC) measures the amount of carbon dioxide produced in the total mineralization of a sample. In both samples (PTi-75 and STi-50) the percentage of TOC was approximately to percentage of degradation of phenol; which means a mineralization of phenol in this reaction time.

3.10. Proposed photodegradation mechanism

A possible mechanism is proposed in order to explain the photocatalytic properties of the p-BiOCl/n-TiO_2 heterojunctions (Figure 13), obtained by sol gel synthesis of TiO_2 nanoparticles with BiOCl. Taking in account when semiconductors are in contact the charges are transferred, so that the Fermi levels eventually reach equilibrium. In addition, the presence of oxygen vacancies, observed in XPS analysis in both photocatalyst, whose electrons located on them have a direct effect on the electronic structure of the composite (BiOCl-TiO_2), since it is generated a donor level below the conduction band and thus can extend the light absorption range to visible light (observed in UV-Vis spectra). These results indicate the shift of the Fermi level of composite toward high energy by oxygen vacancies formation [67–69].

As shown by TRMC experiments, the holes generated in BiOCl are transferred to the valance band of TiO_2 inducing an efficient separation of electron-hole pairs. Meanwhile, the electrons passing from valance band to conduction band go trough a shorter pathway because the generated donor level by the electrons of the oxygen vacancy (represented by the short first red arrow in Figure 13). Therefore, the composite BiOCl-TiO_2 exhibits higher photocatalytic activity.

4. Conclusions

In this study two samples of BiOCl (P2600 and SB) were modified with TiO_2, which was synthesized by the Sol-Gel method. The composite system BiOCl-TiO_2 is very active under visible irradiation, which is not the case of bare TiO_2 or BiOCl. This photocatalytic activity varies with the weight ratio of BiOCl-TiO_2. The PTi-75 composites and Satin BTi-50 showed the highest photocatalytic activity.

Specific planes (001, 101 and 102) of BiOCl crystals are modified in the immediate presence of TiO_2, by secondary interactions, without existing an interstitial substitution. Thus, an overlap of bands can take place enhancing the photocatalytic activity of the composites.

Time resolved conductivity study shows signals under visible excitation at 455 nm for the composites due to the modified band gap of BiOCl. In addition, it can be said that TiO_2 in the heterojunction works as holes traps of the photogenerated holes in BiOCl, decreasing the recombination process. Both free radical ($^{\bullet}OH$) and superoxide ion ($O_2^{\bullet-}$) species are involved in the photocatalytic process, but the contribution of $O_2^{\bullet-}$ is higher. The generated electrons in the conduction band of BiOCl under visible light have a more significant role in the photocatalytic process (compared to the holes) leading to generation of superoxide ions, which ultimately degrade phenol.

During the phenol degradation using these composites under visible irradiation, vacancies of oxygen were observed subsequent to the photocatalytic activity, which changed the energy states of bismuth (Bi^{3+} and Bi^0) and titanium (Ti^{4+} and Ti^{3+}) present in the composites (BiOCl-TiO_2). The obtained photocatalysts, especially the P2600 based one, could be used up to three times with a reasonable efficiency during the phenol photodegradation.

5. Acknowledgements

The authors would thank to MSc. Beatriz Rivera and MSc. Ana Iris Peña from LINAN

(IPICYT) for the support during characterization by SEM and XRD. Dalia Sánchez also thank to CONACYT for the scholarship "Beca Mixta" 296719 and to Université de Paris-Sud for all the support to carry out experiments and characterization in Dr. Hynd's Laboratory.

Appendix A. Supplementary data

References

[1] J.M. Herrmann, C. Duchamp, M. Karkmaz, B.T. Hoai, H. Lachheb, E. Puzenat, C. Guillard, Environmental green chemistry as defined by photocatalysis, J. Hazard. Mater. 146 (2007) 624–629. doi:10.1016/j.jhazmat.2007.04.095.

[2] J. Herrmann, Heterogeneous photocatalysis: fundamentals and applications to the removal of various types of aqueous pollutants, Catal. Today. 53 (1999) 115–129. doi:10.1016/S0920-5861(99)00107-8.

[3] P. Pichat, J. Disdier, C. Hoang-Van, D. Mas, G. Goutailler, C. Gaysse, Purification/deodorization of indoor air and gaseous effluents by TiO2 photocatalysis, Catal. Today. 63 (2000) 363–369. doi:10.1016/S0920-5861(00)00480-6.

[4] D. Schaming, H. Remita, Nanotechnology: from the ancient time to nowadays, Found. Chem. 17 (2015) 187–205. doi:10.1007/s10698-015-9235-y.

[5] L. Zhang, W. Wang, D. Jiang, E. Gao, S. Sun, Photoreduction of CO2 on BiOCl nanoplates with the assistance of photoinduced oxygen vacancies, Nano Res. 8 (2015) 1–11. doi:10.1007/s12274-014-0564-2.

[6] B. Kumar, J.P. Brian, V. Atla, S. Kumari, K.A. Bertram, R.T. White, J.M. Spurgeon, New trends in the development of heterogeneous catalysts for electrochemical CO2 reduction, Catal. Today. 270 (2016) 19–38. doi:10.1016/j.cattod.2016.02.006.

[7] V.P. Indrakanti, J.D. Kubicki, H.H. Schobert, Photoinduced activation of CO2 on Ti-based heterogeneous catalysts: Current state, chemical physics-based insights and outlook, Energy Environ. Sci. 2 (2009) 745–758. doi:10.1039/b822176f.

[8] M. Ni, M.K.H. Leung, D.Y.C. Leung, K. Sumathy, A review and recent developments in photocatalytic water-splitting using TiO2 for hydrogen production, Renew. Sustain. Energy Rev. 11 (2007) 401–425. doi:10.1016/j.rser.2005.01.009.

[9] G. Colón, Towards the hydrogen production by photocatalysis, Appl. Catal. A Gen. 518 (2016) 48–59. doi:10.1016/j.apcata.2015.11.042.

[10] Q. Wang, J. Hui, Y. Huang, Y. Ding, Y. Cai, S. Yin, Z. Li, B. Su, The preparation of BiOCl photocatalyst and its performance of photodegradation on dyes, Mater. Sci. Semicond. Process. 17 (2014) 87–93. doi:10.1016/j.mssp.2013.08.018.

[11] J. He, J. Wang, Y. Liu, Z.A. Mirza, C. Zhao, W. Xiao, Microwave-assisted synthesis of BiOCl and its adsorption and photocatalytic activity, Ceram. Int. 41 (2015) 8028–8033. doi:10.1016/j.ceramint.2015.02.152.

[12] J. Jin, Y. Wang, T. He, Preparation of thickness-tunable BiOCl nanosheets with high photocatalytic activity for photoreduction of CO2, RSC Adv. 5 (2015) 100244–100250. doi:10.1039/C5RA21888H.

[13] L. Ye, Y. Su, X. Jin, H. Xie, C. Zhang, Recent advances in BiOX (X = Cl, Br and I) photocatalysts: synthesis, modification, facet effects and mechanisms, Environ. Sci. Nano. 1 (2014) 90. doi:10.1039/c3en00098b.

[14] H. Cheng, B. Huang, Y. Dai, Engineering BiOX (X = Cl, Br, I) nanostructures for highly efficient photocatalytic applications, Nanoscale. 6 (2014) 2009. doi:10.1039/c3nr05529a.

[15] Y. Zhiyong, D. Bahnemann, R. Dillert, S. Lin, L. Liqin, Photocatalytic degradation of azo dyes by BiOX (X=Cl, Br), J. Mol. Catal. A Chem. 365 (2012) 1–7. doi:10.1016/j.molcata.2012.07.001.

[16] L. Ye, X. Jin, Y. Leng, Y. Su, H. Xie, C. Liu, Synthesis of black ultrathin BiOCl nanosheets for efficient photocatalytic H2 production under visible light irradiation, J. Power Sources. 293 (2015) 409–415. doi:10.1016/j.jpowsour.2015.05.101.

[17] Y. Wang, Z.Q. Shi, C.M. Fan, X.G. Hao, G.Y. Ding, Y.F. Wang, Synthesis of BiOCl photocatalyst by a low-cost, simple hydrolytic technique and its excellent photocatalytic activity, Int. J. Miner. Metall. Mater. 19 (2012) 467–472. doi:10.1007/s12613-012-0581-7.

[18] B. Sarwan, B. Pare, A.D. Acharya, The effect of oxygen vacancies on the photocatalytic activity of BiOCl nanocrystals prepared by hydrolysis and UV light irradiation, Mater. Sci. Semicond. Process. 25 (2014) 89–97. doi:10.1016/j.mssp.2013.09.015.

[19] K. Li, Y. Liang, J. Yang, Q. Gao, Y. Zhu, S. Liu, R. Xu, X. Wu, Controllable

synthesis of {001} facet dependent foursquare BiOCl nanosheets: A high efficiency photocatalyst for degradation of methyl orange, J. Alloys Compd. 695 (2017) 238–249. doi:10.1016/j.jallcom.2016.10.204.

[20] J. Li, Y. Zhu, Y. Yan, B. Xi, K. Tang, Y. Qian, Solvothermal Synthesis of 3D BiOCl Microstructures and Their Electrochemical Hydrogen Storage Behavior, J. Nanosci. Nanotechnol. 12 (2012). doi:10.1166/jnn.2012.5673.

[21] D. Sun, J. Li, Z. Feng, L. He, B. Zhao, T. Wang, R. Li, S. Yin, T. Sato, Solvothermal synthesis of BiOCl flower-like hierarchical structures with high photocatalytic activity, Catal. Commun. 51 (2014) 1–4. doi:10.1016/j.catcom.2014.03.004.

[22] X. Chang, M.A. Gondal, A.A. Al-Saadi, M.A. Ali, H. Shen, Q. Zhou, J. Zhang, M. Du, Y. Liu, G. Ji, Photodegradation of Rhodamine B over unexcited semiconductor compounds of BiOCl and BiOBr, J. Colloid Interface Sci. 377 (2012) 291–298. doi:10.1016/j.jcis.2012.03.021.

[23] T. Xie, L. Xu, C. Liu, J. Yang, M. Wang, Magnetic composite BiOCl–SrFe 12 O 19 : a novel p–n type heterojunction with enhanced photocatalytic activity, Dalt. Trans. 43 (2014) 2211–2220. doi:10.1039/C3DT52219A.

[24] J. Jiang, K. Zhao, X. Xiao, L. Zhang, Synthesis and facet-dependent photoreactivity of BiOCl single-crystalline nanosheets, J. Am. Chem. Soc. 134 (2012) 4473–4476. doi:10.1021/ja210484t.

[25] Y. Ao, H. Tang, P. Wang, C. Wang, Deposition of Ag@AgCl onto two dimensional square-like BiOCl nanoplates for high visible-light photocatalytic activity, Mater. Lett. 131 (2014) 74–77. doi:10.1016/j.matlet.2014.05.083.

[26] W. Zhu, Z. Li, Y. Zhou, X. Yan, Deposition of silver nanoparticles onto two dimensional BiOCl nanodiscs for enhanced visible light photocatalytic and biocidal activities, Rsc Adv. 6 (2016) 64911–64920. doi:10.1039/c6ra09964e.

[27] Z. Zhang, Y. Zhou, S. Yu, M. Chen, F. Wang, Ag-BiOCl nanocomposites prepared by the oxygen vacancy induced photodeposition method with improved visible light photocatalytic activity, Mater. Lett. 150 (2015) 97–100. doi:10.1016/j.matlet.2015.03.011.

[28] J. Xia, Improved visible light photocatalytic properties of Fe/BiOCl microspheres synthesized via self-doped reactable ionic liquids †, (2013) 10132–10141. doi:10.1039/c3ce41555d.

[29] L. Yang, Y. Xingzhong, W. Hou, C. Xiaohong, G. Shansi, J. Qian, W. Zhibin, J.

Longbo, Z. Guangming, Solvothermal synthesis of graphene/BiOCl0.75Br0.25 microspheres with excellent visible-light photocatalytic activity, RSC Adv. 5 (2015) 33696–33704. doi:10.1039/c5ra02852c.

[30] F. Gao, D. Zeng, Q. Huang, S. Tian, C. Xie, Chemically bonded graphene/BiOCl nanocomposites as high-performance photocatalysts, Phys. Chem. Chem. Phys. 14 (2012) 10572. doi:10.1039/c2cp41045a.

[31] S. Kang, R.C. Pawar, Y. Pyo, V. Khare, C.S. Lee, Size-controlled BiOCl–RGO composites having enhanced photodegradative properties, J. Exp. Nanosci. 8080 (2015) 1–17. doi:10.1080/17458080.2015.1047420.

[32] S. Jiang, K. Zhou, Y. Shi, S. Lo, H. Xu, Y. Hu, Z. Gui, In situ synthesis of hierarchical flower-like Bi2S3/BiOCl composite with enhanced visible light photocatalytic activity, Appl. Surf. Sci. 290 (2014) 313–319. doi:10.1016/j.apsusc.2013.11.074.

[33] S.Y. Chai, Y.J. Kim, M.H. Jung, A.K. Chakraborty, D. Jung, W.I. Lee, Heterojunctioned BiOCl/Bi2O3, a new visible light photocatalyst, J. Catal. 262 (2009) 144–149. doi:10.1016/j.jcat.2008.12.020.

[34] X. Zhang, T. Guo, X. Wang, Y. Wang, C. Fan, H. Zhang, Facile composition-controlled preparation and photocatalytic application of BiOCl/Bi2O2CO3 nanosheets, Appl. Catal. B Environ. 150–151 (2014) 486–495. doi:10.1016/j.apcatb.2013.12.054.

[35] L. Li, M. Zhang, Y. Liu, X. Zhang, Hierarchical assembly of BiOCl nanosheets onto bicrystalline TiO2 nanofiber: Enhanced photocatalytic activity based on photoinduced interfacial charge transfer, J. Colloid Interface Sci. 435 (2014) 26–33. doi:10.1016/j.jcis.2014.08.022.

[36] R. Fu, X. Zeng, L. Ma, S. Gao, Q. Wang, Z. Wang, B. Huang, Y. Dai, J. Lu, Enhanced photocatalytic and photoelectrochemical activities of reduced TiO2-x/BiOCl heterojunctions, J. Power Sources. 312 (2016) 12–22. doi:10.1016/j.jpowsour.2016.02.038.

[37] J. Yang, X. Wang, X. Lv, X. Xu, Y. Mi, J. Zhao, Preparation and photocatalytic activity of BiOX-TiO2 composite films (X=Cl, Br, I), Ceram. Int. 40 (2014) 8607–8611. doi:10.1016/j.ceramint.2014.01.077.

[38] M. Guerrero, A. Altube, E. García-Lecina, E. Rossinyol, M.D. Baró, E. Pellicer, J. Sort, Facile in situ synthesis of BiOCl nanoplates stacked to highly porous TiO2: A synergistic combination for environmental remediation, ACS Appl.

Mater. Interfaces. 6 (2014) 13994–14000. doi:10.1021/am5033549.

[39] Z. Liu, X. Xu, J. Fang, X. Zhu, B. Li, Synergistic degradation of eosin y by photocatalysis and electrocatalysis in UV irradiated solution containing hybrid BiOCl/TiO 2 particles, Water. Air. Soil Pollut. 223 (2012) 2783–2798. doi:10.1007/s11270-011-1066-4.

[40] D. Sun, J. Li, L. He, B. Zhao, T. Wang, R. Li, S. Yin, Z. Feng, T. Sato, Facile solvothermal synthesis of BiOCl–TiO2 heterostructures with enhanced photocatalytic activity, CrystEngComm. 16 (2014) 7564. doi:10.1039/C4CE00596A.

[41] L. Zhang, J. Zhang, W. Zhang, J. Liu, H. Zhong, Y. Zhao, Photocatalytic activity of attapulgite-BiOCl-TiO2 toward degradation of methyl orange under UV and visible light irradiation, Mater. Res. Bull. 66 (2015) 109–114. doi:10.1016/j.materresbull.2015.02.029.

[42] B. Pare, B. Sarwan, S.B. Jonnalagadda, Photocatalytic mineralization study of malachite green on the surface of Mn-doped BiOCl activated by visible light under ambient condition, Appl. Surf. Sci. 258 (2011) 247–253. doi:10.1016/j.apsusc.2011.08.040.

[43] F. Chen, H. Liu, S. Bagwasi, X. Shen, J. Zhang, Photocatalytic study of BiOCl for degradation of organic pollutants under UV irradiation, J. Photochem. Photobiol. A Chem. 215 (2010) 76–80. doi:10.1016/j.jphotochem.2010.07.026.

[44] C. Huang, J. Hu, S. Cong, Z. Zhao, X. Qiu, Hierarchical BiOCl microflowers with improved visible-light-driven photocatalytic activity by Fe(III) modification, Appl. Catal. B Environ. 174–175 (2015) 105–112. doi:10.1016/j.apcatb.2015.03.001.

[45] X. Zhang, Z. Ai, F. Jia, L. Zhang, Generalized one-pot synthesis, characterization, and photocatalytic activity of hierarchical BiOX (X = Cl, Br, I) nanoplate microspheres, J. Phys. Chem. C. 112 (2008) 747–753. doi:10.1021/jp077471t.

[46] I. Ali, S.-R. Kim, S.-P. Kim, J.-O. Kim, Anodization of bismuth doped TiO2 nanotubes composite for photocatalytic degradation of phenol in visible light, Catal. Today. 282 (2017) 31–37. doi:10.1016/j.cattod.2016.03.029.

[47] J. Zhang, Y. Du, L. Zhang, X. Zheng, Y. Ma, S. Dong, D. Zhou, Preparation of sponge carrier supported photocatalyst by self-assembly technique for phenol photodegradation in visible light, Mol. Catal. 432 (2017) 1–7.

doi:10.1016/j.mcat.2017.01.022.

[48] M.K. Renuka, V. Gayathri, UV/solar light induced photocatalytic degradation of phenols and dyes by Fe(PS-BBP)Cl 3, J. Photochem. Photobiol. A Chem. (2017). doi:10.1016/j.jphotochem.2017.12.012.

[49] Q. Li, D. Zhou, P. Zhang, P. Man, Z. Tian, Y. Li, S. Ai, The BiOBr/regenerated cellulose composite film as a green catalyst for light degradation of phenol, Colloids Surfaces A Physicochem. Eng. Asp. 501 (2016) 132–137. doi:10.1016/j.colsurfa.2016.04.054.

[50] M.A. Mohamed, W.N.W. Salleh, J. Jaafar, A.F. Ismail, N.A.M. Nor, Photodegradation of phenol by N-Doped TiO2 anatase/rutile nanorods assembled microsphere under UV and visible light irradiation, Mater. Chem. Phys. 162 (2015) 113–123. doi:10.1016/j.matchemphys.2015.05.033.

[51] J. Yao, H. Chen, F. Jiang, Z. Jiao, M. Jin, Titanium dioxide and cadmium sulfide co-sensitized graphitic carbon nitride nanosheets composite photocatalysts with superior performance in phenol degradation under visible-light irradiation, J. Colloid Interface Sci. 490 (2017) 154–162. doi:10.1016/j.jcis.2016.11.051.

[52] Z.J. Wu, W. Huang, K.K. Cui, Z.F. Gao, P. Wang, Sustainable synthesis of metals-doped ZnO nanoparticles from zinc-bearing dust for photodegradation of phenol, J. Hazard. Mater. 278 (2014) 91–99. doi:10.1016/j.jhazmat.2014.06.001.

[53] L. Zhang, J. Zhang, W. Zhang, J. Liu, H. Zhong, Y. Zhao, Photocatalytic activity of attapulgite–BiOCl–TiO2 toward degradation of methyl orange under UV and visible light irradiation, 66 (2015) 109–114. doi:10.1016/j.materresbull.2015.02.029.

[54] W. Li, T. Yi, Li Huan, C. Zhao, Z. Baoliang, Z. Hepeng, G. Wangchang, Zhang Qiuyu, Novel BiOCl-TiO2 hierarchical composites: synthesis, characterization and application on photocatalysis, Appl. Catal. A Gen. 516 (2016) 81–89.

[55] F. Duo, Y. Wang, C. Fan, X. Mao, X. Zhang, Y. Wang, J. Liu, Low temperature one-step synthesis of rutile TiO2/BiOCl composites with enhanced photocatalytic activity, Mater. Charact. 99 (2015) 8–16. doi:10.1016/j.matchar.2014.11.002.

[56] Y. Ao, J. Bao, P. Wang, C. Wang, J. Hou, Bismuth oxychloride modified titanium phosphate nanoplates: A new p-n type heterostructured photocatalyst with high activity for the degradation of different kinds of organic pollutants, J. Colloid Interface Sci. 476 (2016) 71–78. doi:10.1016/j.jcis.2016.05.021.

[57] L. Tian, J. Liu, C. Gong, L. Ye, L. Zan, Fabrication of reduced graphene oxide-

BiOCl hybrid material via a novel benzyl alcohol route and its enhanced photocatalytic activity, J. Nanoparticle Res. 15 (2013). doi:10.1007/s11051-013-1917-6.

[58] L. Zhang, W. Wang, D. Jiang, E. Gao, S. Sun, Photoreduction of CO2 on BiOCl nanoplates with the assistance of photoinduced oxygen vacancies, Nano Res. 8 (2015) 821–831. doi:10.1007/s12274-014-0564-2.

[59] X. Wang, Q. Ni, D. Zeng, G. Liao, Y. Wen, B. Shan, C. Xie, BiOCl/TiO2 heterojunction network with high energy facet exposed for highly efficient photocatalytic degradation of benzene, Appl. Surf. Sci. 396 (2017) 590–598. doi:10.1016/j.apsusc.2016.10.201.

[60] H. Li, J. Shi, K. Zhao, L. Zhang, Sustainable molecular oxygen activation with oxygen vacancies on the {001} facets of BiOCl nanosheets under solar light, Nanoscale. 6 (2014) 14168–14173. doi:10.1039/C4NR04810E.

[61] C. Colbeau-Justin, M. Kunst, D. Huguenin, Structural influence on charge-carrier lifetimes in TiO2 powders studied by microwave absorption, J. Mater. Sci. 38 (2003) 2429–2437. doi:10.1023/A:1023905102094.

[62] A.R. Hassan, Two-Photon Absorption in an Indirect-Gap Semiconductor Quantum Well System. I. Interband Transitions, Phys. Status Solidi. 184 (1994) 519–528.

[63] A. Goetzberger, J. Knobloch, B. Voss, Crystalline silicon solar cells, Editor. John Wiley Sons Ltd. 1 (1998).

[64] I.D. Sharma, G.K. Tripathi, V.K. Sharma, S.N. Tripathi, R. Kurchania, C. Kant, A.K. Sharma, K.K. Saini, One-pot synthesis of three bismuth oxyhalides (BiOCl, BiOBr, BiOI) and their photocatalytic properties in three different exposure conditions, Cogent Chem. 1 (2015) 1–15. doi:10.1080/23312009.2015.1076371.

[65] Y. Zhao, X. Huang, X. Tan, T. Yu, X. Li, L. Yang, S. Wang, Fabrication of BiOBr nanosheets@TiO2 nanobelts p-n junction photocatalysts for enhanced visible-light activity, Appl. Surf. Sci. 365 (2016) 209–217. doi:10.1016/j.apsusc.2015.12.249.

[66] J. Li, Y. Yu, L. Zhang, Bismuth oxyhalide nanomaterials: layered structures meet photocatalysis, Nanoscale. 6 (2014) 8473. doi:10.1039/C4NR02553A.

[67] X. Pan, M.-Q. Yang, X. Fu, N. Zhang, Y.-J. Xu, Defective TiO2 with oxygen vacancies: synthesis, properties and photocatalytic applications, Nanoscale. 5 (2013) 3601. doi:10.1039/c3nr00476g.

[68] L. Ye, H. Wang, X. Jin, Y. Su, D. Wang, H. Xie, X. Liu, X. Liu, Synthesis of olive-green few-layered BiOI for efficient photoreduction of CO2 into solar fuels under visible/near-infrared light, Sol. Energy Mater. Sol. Cells. 144 (2016) 732–739. doi:10.1016/j.solmat.2015.10.022.

[69] Y. Li, C. Li, Z. Zhang, Y. Zhang, X. Sun, H. Si, J. Zhang, Black BiOCl with disorder surface structure prepared by Fe reduction and the enhanced photocatalytic activity, Solid State Sci. 34 (2014) 107–112. doi:10.1016/j.solidstatesciences.2014.05.011.

Figures caption

Figure 1. X-ray diffraction (XRD) patterns of pure BiOCl (P2600 and SB), pure TiO2 and BiOCl-TiO2 composite with different amount of TiO2. a) P2600-TiO2 and b) SB-TiO2.

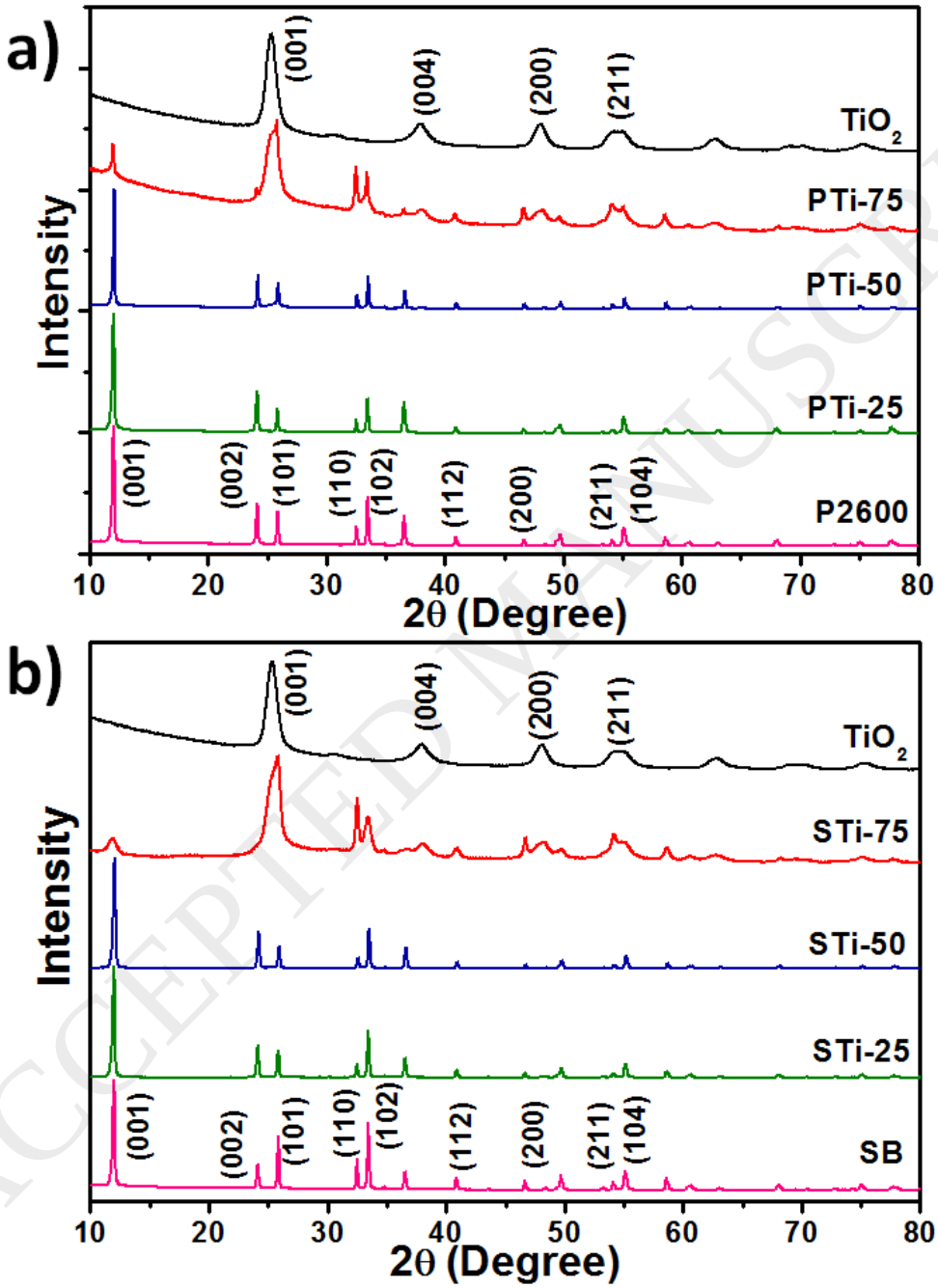

Figure 2. SEM images of pure parent reagents and BiOCl-TiO2 composites. a)Pure TiO2, b)Pure P2600, c)PTi-75, d) STi-50, e and f) PTi-75.

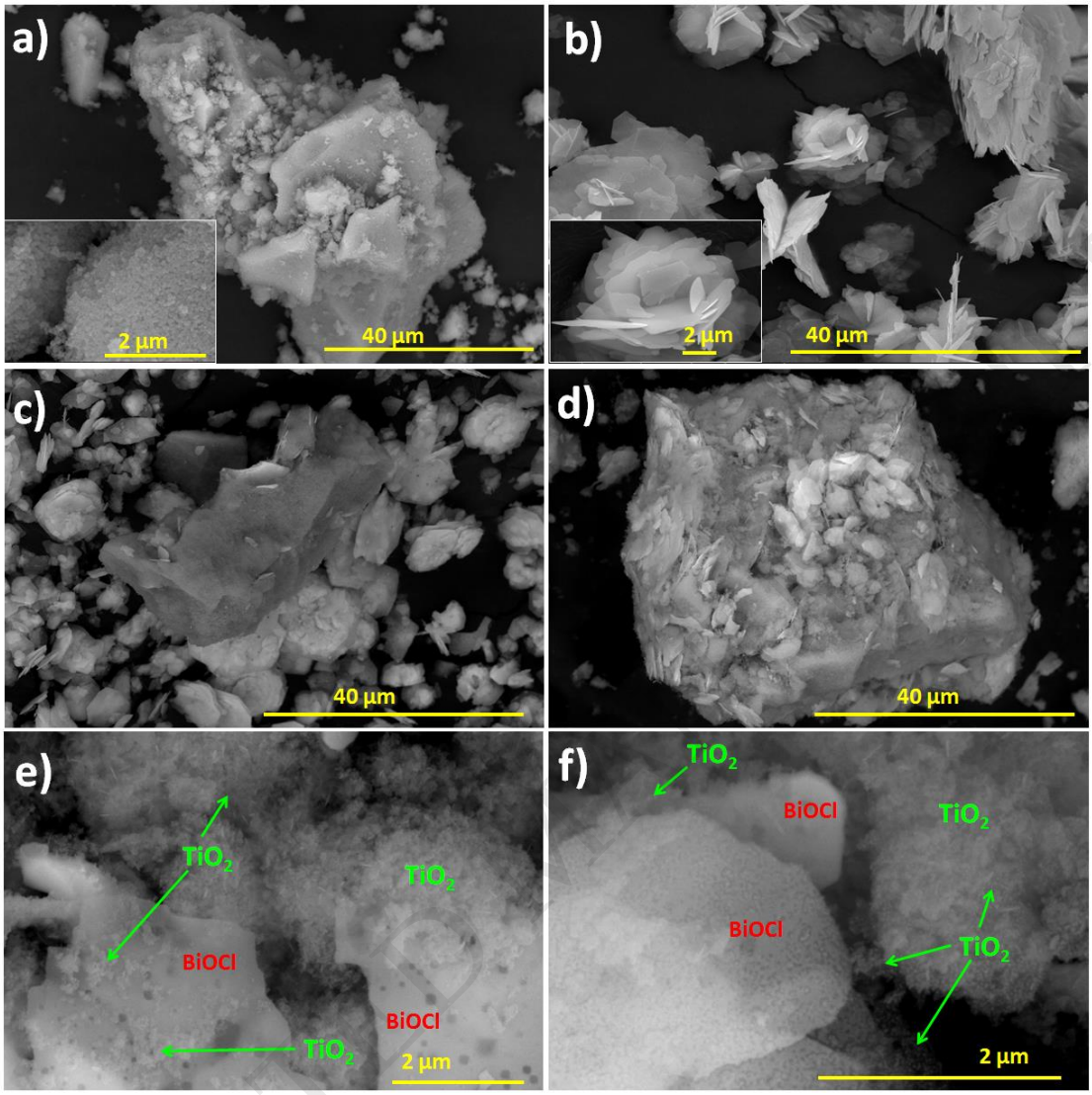

Figure 3. EDS analysis of Pearl-TiO2 sample.

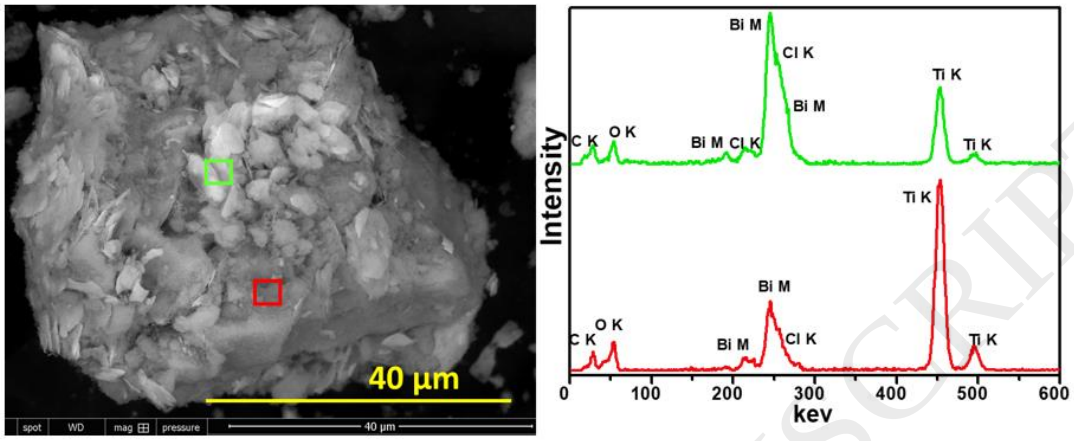

Figure 4. TEM and HRTEM images of the BiOCl-TiO2 samples obtained. a and b) PTi-75, c and d) STi-50.

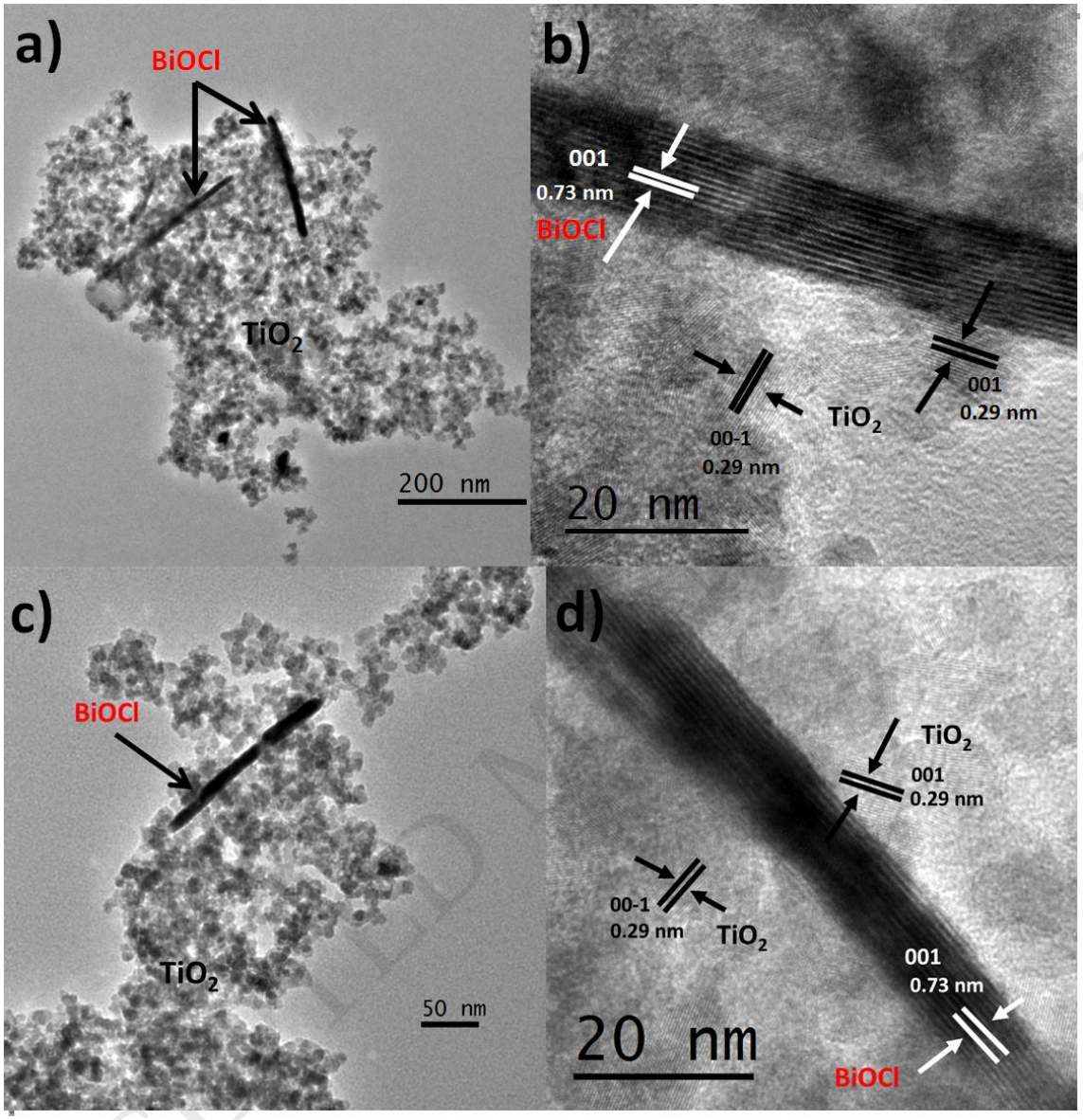

Figure 5. FT-IR spectra of pure BiOCl (P2600 and SB), pure TiO2 and BiOCl-TiO2 composites: a) P2600-TiO2 and b) SB-TiO2.

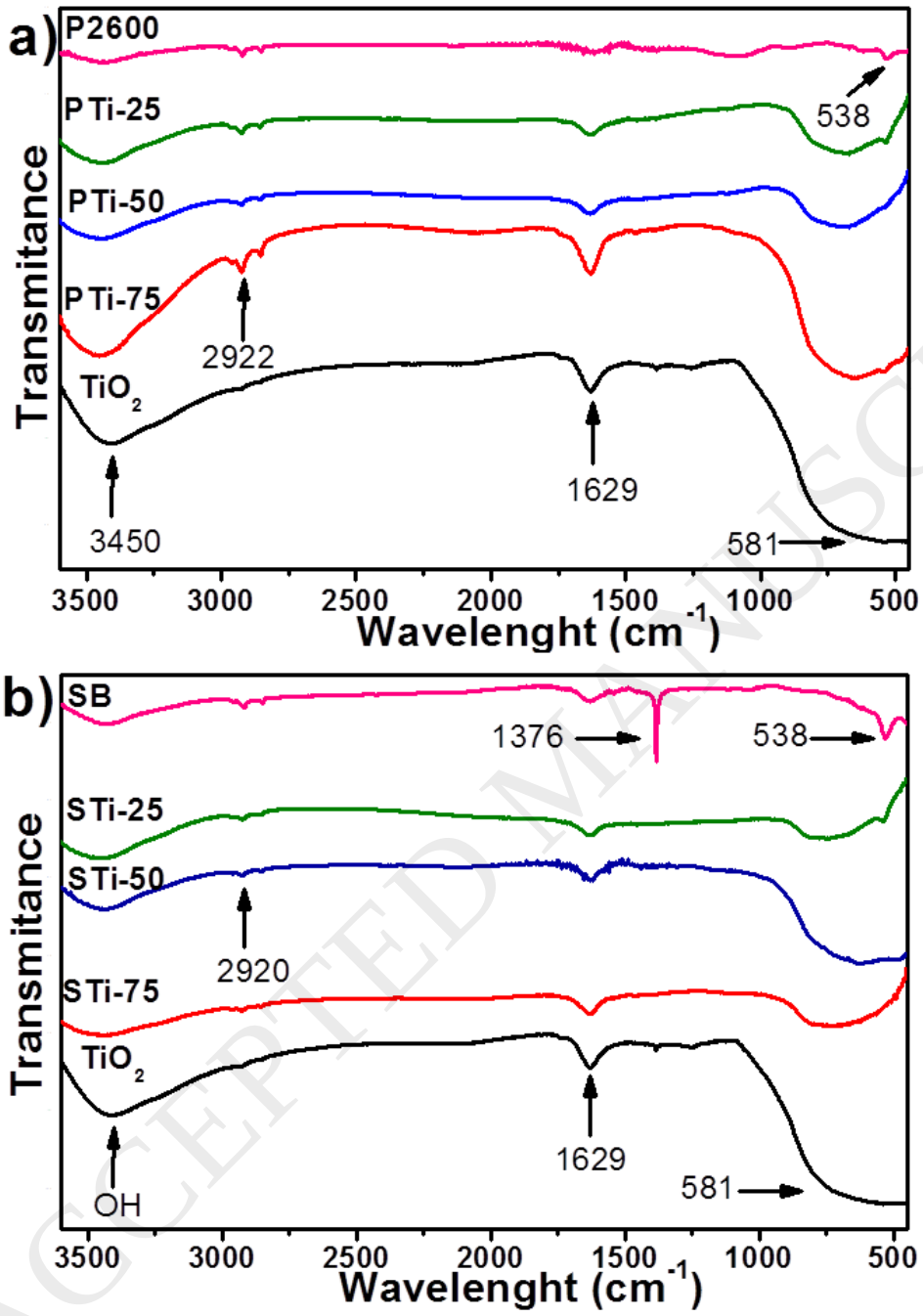

Figure 6. UV-Vis spectra for pure BiOCl (P2600 and SB), pure TiO2 and BiOCl-TiO2 composites: a) P2600-TiO2 and b) SB-TiO2.

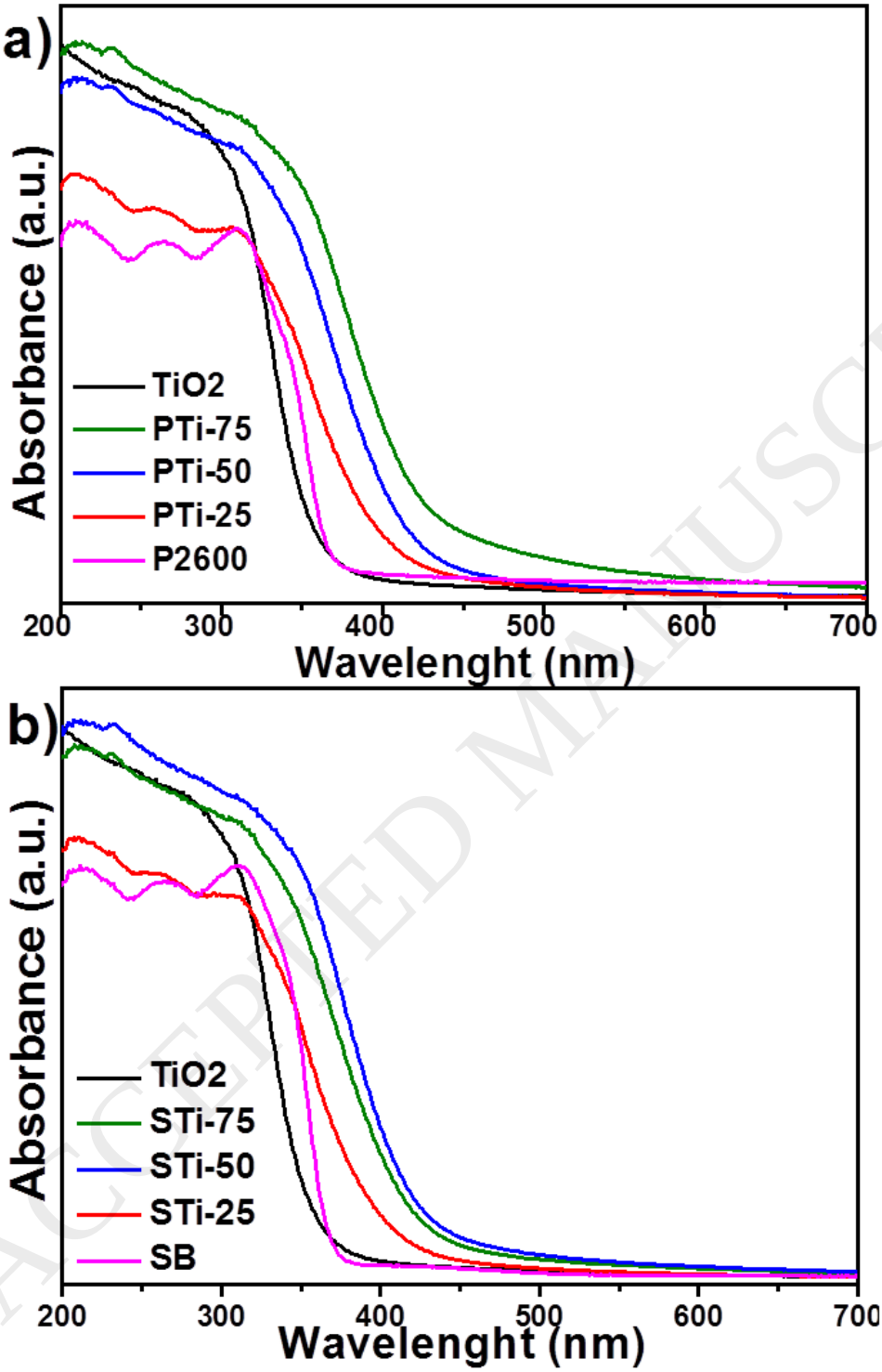

Figure 7. Phenol degradation under visible irradiation (450 nm). I) P2600-TiO2 and II) SB-TiO2.

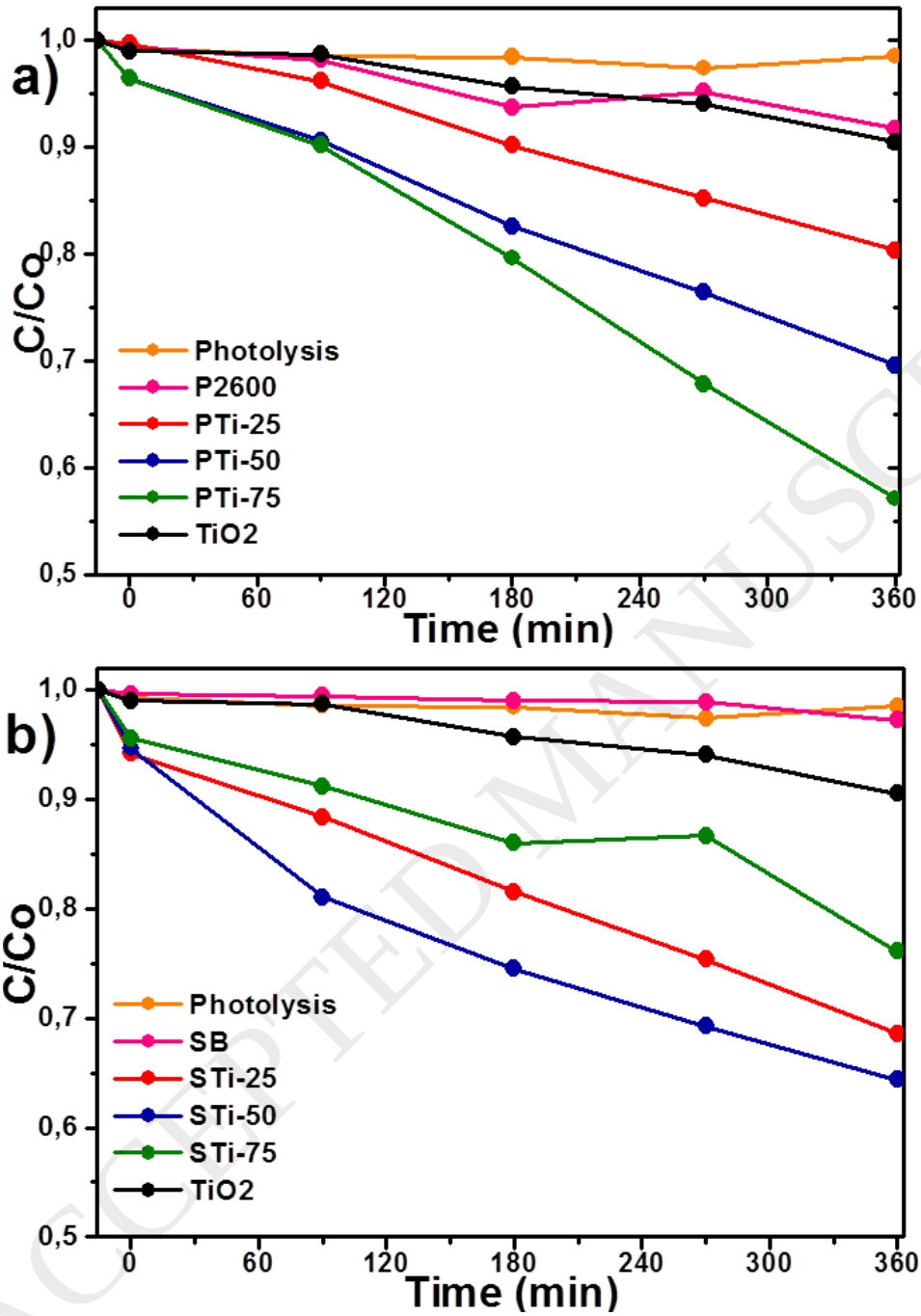

Figure 8. XPS spectra of P2600 pure (a and b), PTi-75 composite (c, d and c) and TiO2 pure (f and g).

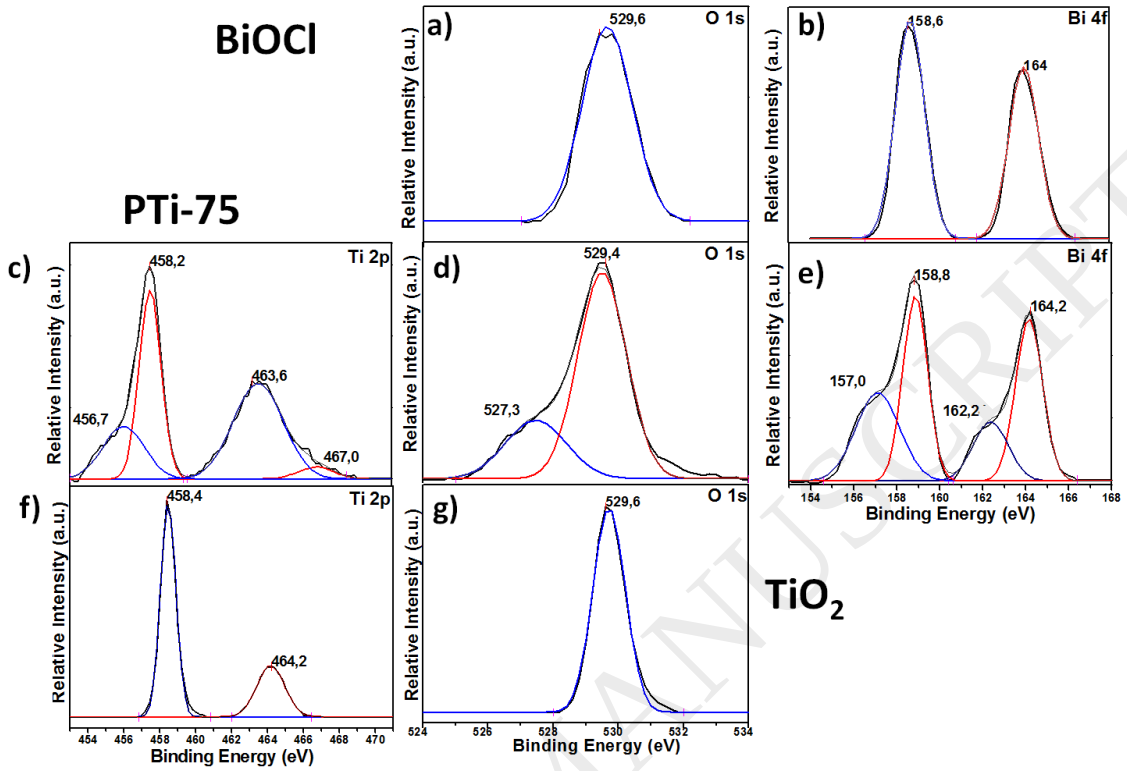

Figure 9. XPS spectra of SB pure (a and b), PTi-75 composite (c, d and c) and TiO2 pure (f and g).

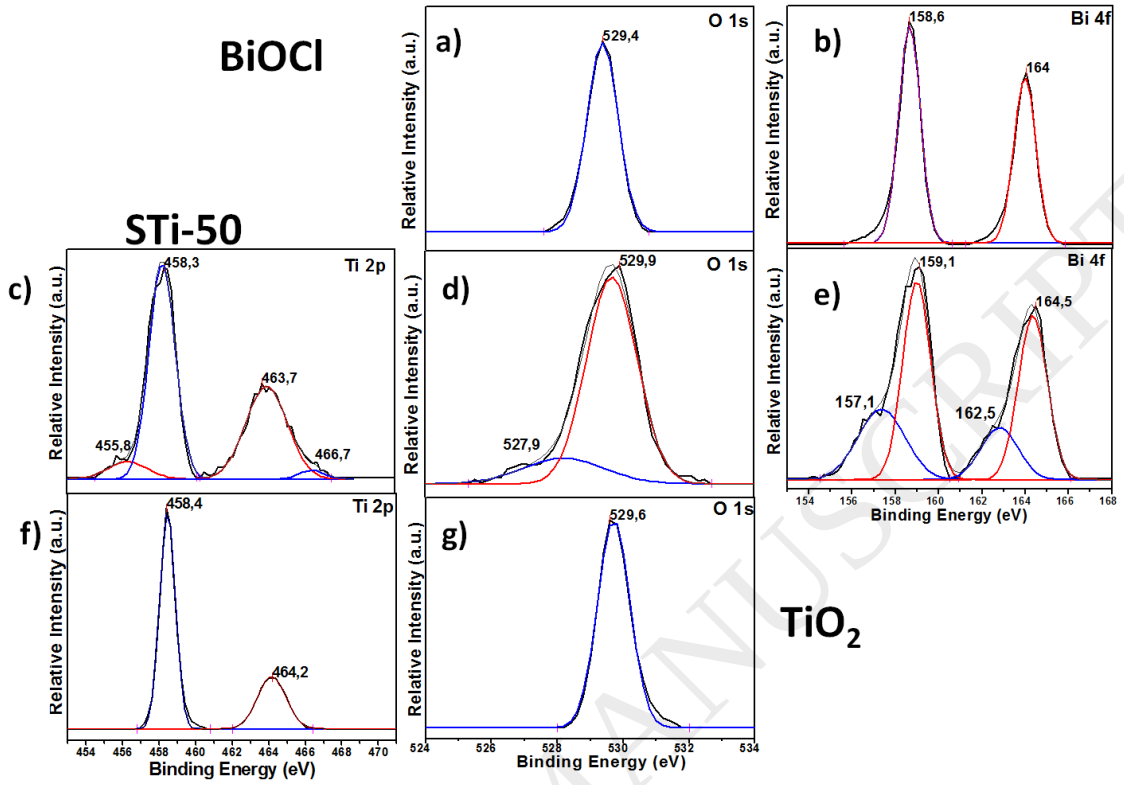

Figure 10. TRMC signals at 455 nm for the BiOCl-TiO2 composites. a) PTi-75, b) STi-50 and c) Scheme of the recombination process band gaps and band positions of TiO2 and BiOCl values taken from Marshall 2014 and Zhao 2014.

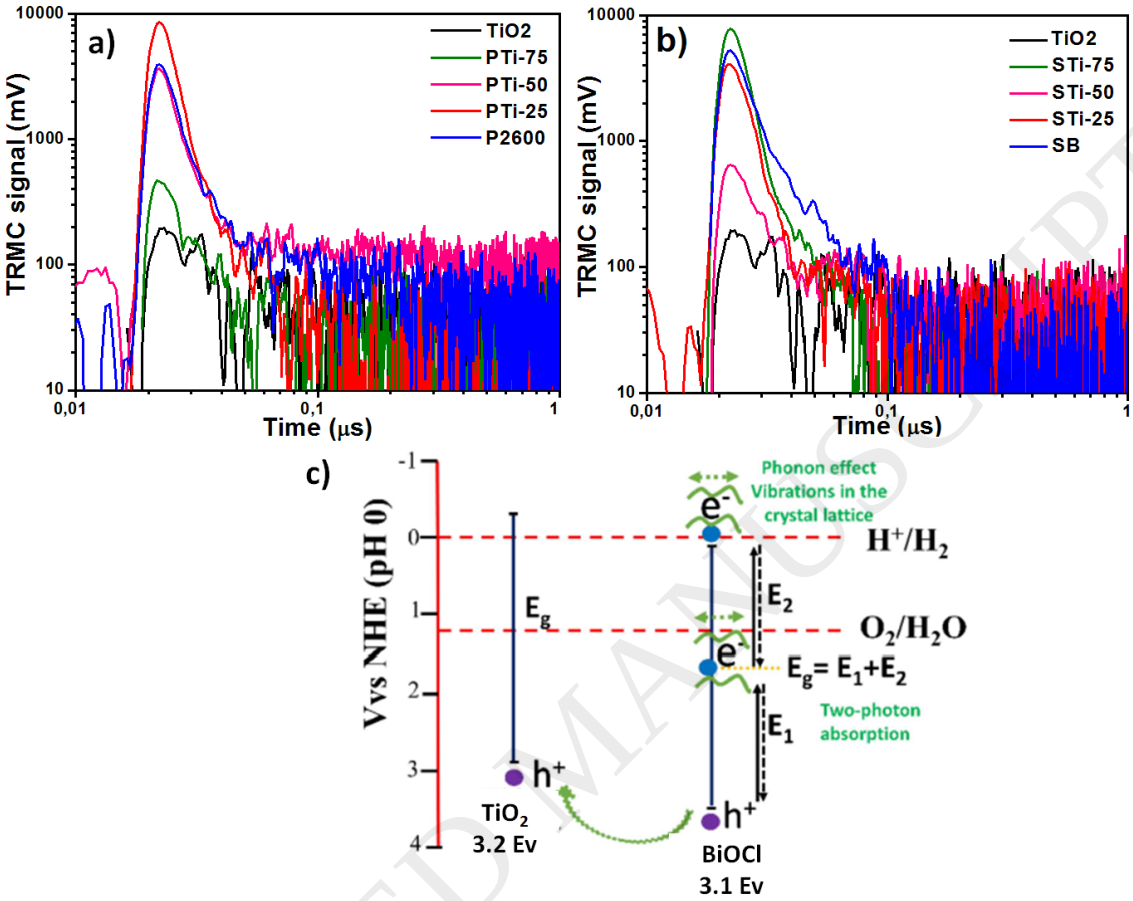

Figure 11. Phenol degradation using PTi-75 in presence of electrons (CuSO4) and holes traps (IPA).

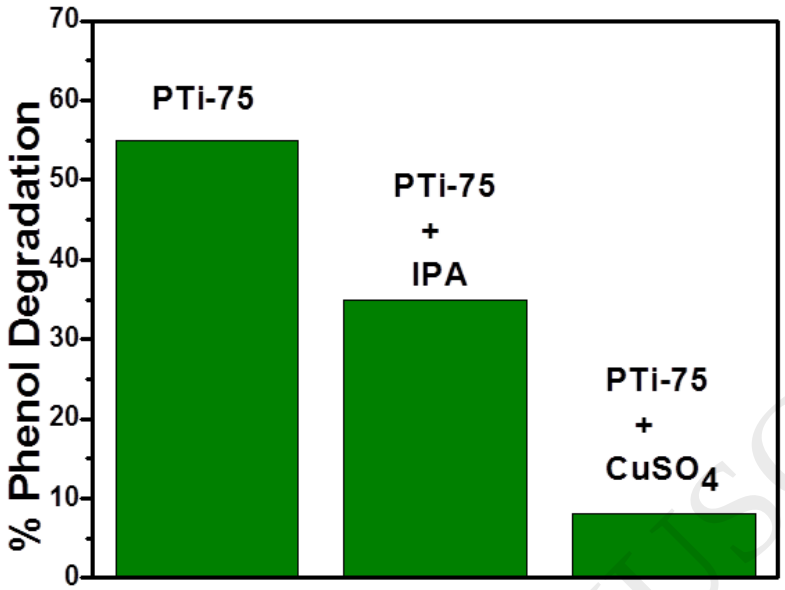

Figure 12. Photocatalytic measurement of BiOCl-TiO2 composites (PTi-75 and STi-50) under visible irradiation for 3 cycles.

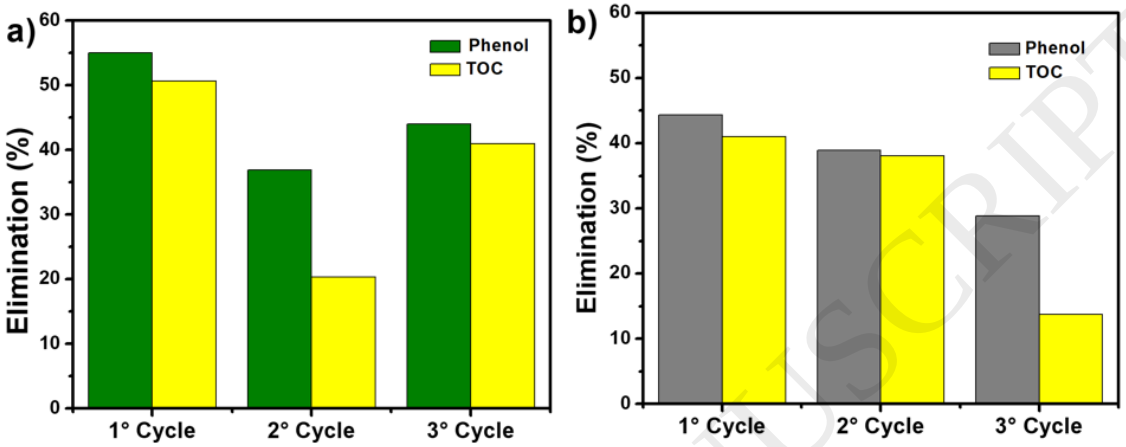

Figure 13. Proposed mechanism for the TiO2- BiOCl composites.

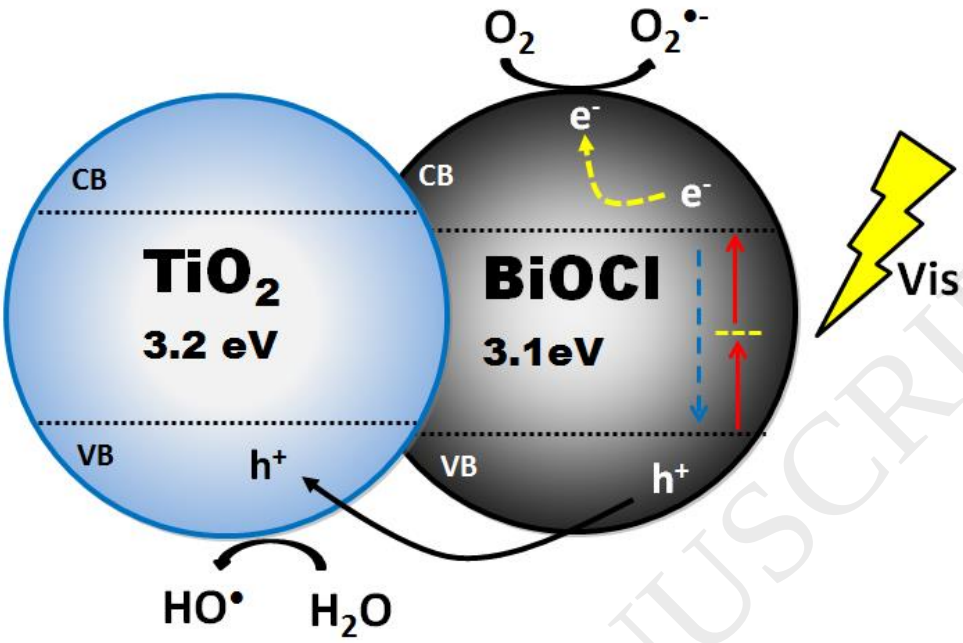

Tables

Table 1. BiOCl-TiO_2 w/w ratios.

Sample ID	Percentage by weight % Pearl 2600	TiO_2	Sample ID	Percentage by weight % Satin B	TiO_2
P2600	100*	0	SB	100*	0
PTi-25	75	25	STi-25	75	25
PTi-50	50	50	STi-50	50	50
PTi-75	25	75	STi-25	25	75
TiO_2	0	100**	TiO_2	0	100**

*BiOCl sample calcined at 450 ºC **TiO_2 sample obtained to sol-gel method

Table 2. Band gap for BiOCl-TiO_2, BiOCl and TiO_2.

Sample ID	Band Gap (eV)	Sample ID	Band Gap (eV)
P2600	3.1	SB	3.1
PTi-25	3.0	STi-25	3.0
PTi-50	2.9	STi-50	2.8
PTi-75	2.8	STi-75	2.9
TiO_2	3.2	TiO_2	3.2

Table 3. Some works related to phenol photodegradation

Photo catalyst	Phenol	Characteristics	% Degradation	Reference
Er^{3+}:$YAlO_3$/TiO_2 : 0,39 g	50mgL^{-1}	λ=455 nm Vis	58% (8 h)	[47]
Fe(PS-BBP)Cl_3: 70 mg	20 mgL^{-1}	λ=250-350 nm UV	96% (30 min)	[48]
BiOBr/RC: 25 mg	7 mgL^{-1}	λ=420 nm Vis	80% (3 h)	[49]
N-doped TiO_2: 0,3 g	50mgL^{-1}	λ=312 nm UV	99,6% (540 min)	[50]
N-doped TiO_2: 0,4 g	50mgL^{-1}	λ=420 nm Vis	99,2% (540 min)	[50]
TiO_2-CdS-gCNNSs: 50 mg	10mgL^{-1}	λ=420 nm Vis	80% (300 min)	[51]
M-ZnO	25mgL^{-1}	λ=400 nm Vis	61.8% (200 min)	[52]